Automatic detection and localization of Focal Cortical Dysplasia lesions in MRI using fully convolutional neural network

K.M. Bijay Dev [a], Pawan S. Jogi [a], S. Niyas [a], S. Vinayagamani [b],
Chandrasekharan Kesavadas [b], Jeny Rajan [a],*

[a] Department of Computer Science and Engineering, National Institute of Technology Karnataka, Surathkal, India
[b] Department of Imaging Sciences and Interventional Radiology, Sree Chitra Tirunal Institute for Medical Sciences and Technology, Trivandrum, India

ARTICLE INFO

ABSTRACT

Focal cortical dysplasia (FCD) is the leading cause of drug-resistant epilepsy in both children and adults. At present, the only therapeutic approach in patients with drug-resistant epilepsy is surgery. Hence, the quantification of FCD via non-invasive imaging techniques helps physicians to decide on surgical interventions. The properties like non-invasiveness and capability to produce high-resolution images makes magnetic resonance imaging an ideal tool for detecting the FCD to an extent. The FCD lesions vary in size, shape, and location for different patients and make the manual detection time consuming and sensitive to the experience of the observer. Automatic segmentation of FCD lesions is challenging due to the difference in signal strength in images acquired with different machines, noise, and other kinds of distortions such as motion artifacts. Most of the methods proposed in the literature use conventional machine learning and image processing techniques in which their accuracy relies on the trained features. Hence, feature extraction should be done more precisely which requires human expertise. The ability to learn the appropriate features/representations from the training data without any human interventions makes the convolutional neural network (CNN) the suitable method for addressing these drawbacks. As far as we are aware, this work is the first one to use a CNN based model to solve the aforementioned problem using only MRI FLAIR images. We customized the popular U-Net architecture and trained the proposed model from scratch (using MRI images acquired with 1.5T and 3T scanners). FCD detection rate (recall) of the proposed model is 82.5 (33/40 patients detected correctly).

© 2019 Elsevier Ltd. All rights reserved.

1. Introduction

Epilepsy is a neurological disease that affects the functioning of the nervous system. It is characterized by repeated epileptic seizures, and hence it is also known as a seizure disorder. Current statistics show that about 65 million people in the world suffer from epilepsy [1]. Focal cortical dysplasia (FCD) is an abnormality of cortical development and a major cause of drug-resistant epilepsy in both children and adults [2,3]. The major consequence of FCD are seizures, but previous studies in the literature show that FCD may directly contribute to cognitive impairments such as the decline in verbal ability, motor function, or vision [3]. At present, the only treatment for patients with drug-resistant epilepsy is surgery. But only 60–70% achieves complete seizure-freedom after the surgery

[4–6]. This can be improved by using methods that can detect the true extent of lesions effectively.

The properties like non-invasiveness, non-ionizing radiation and the capability to produce high-resolution images make magnetic resonance imaging an ideal tool for detecting the FCD to an extent [3,7,8]. Mainly, features like cortical thickening, blurring of gray matter-white matter junction, increased fluid-attenuated inversion recovery (FLAIR) signal intensity in the thickened cortex and adjacent subcortical white matter in MR images are used to characterize FCD lesions [9]. However, FCD lesions are generally small and subtle which makes the manual tracing time consuming and it is also sensitive to observer variability. Moreover, most subtle FCD lesions are undetected in the routine MRI checkup. In such contexts, automated methods for FCD detection and quantification can be of great assistance to the neuroradiologist.

Several automatic FCD detection methods are proposed in the literature. FCD lesion detection methods can be mainly categorized into brain symmetry based approaches, template- based approaches and feature-based approaches [10]. In brain symmetry-

* Corresponding author.
E-mail addresses: jenyrajan@gmail.com, jenyrajan@nitk.edu.in (J. Rajan).

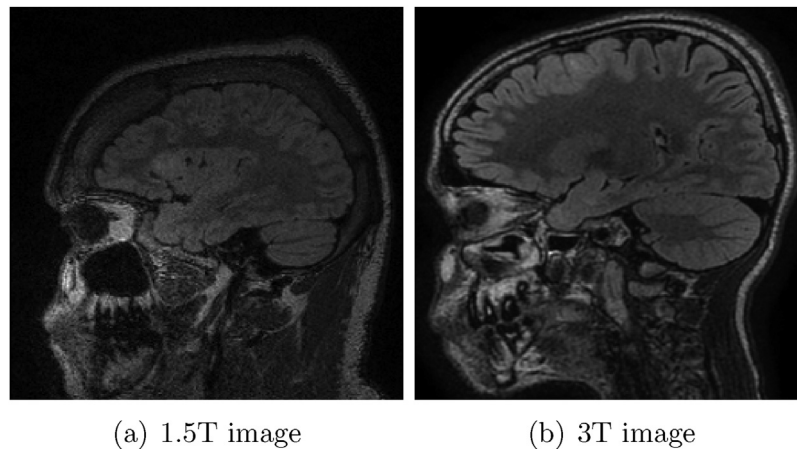(a) 1.5T image　　　　　　　　(b) 3T image

Fig. 1. Sample MRI-scans of brain acquired with 1.5T and 3T scanners. The difference in signal to noise ratio (SNR) can be observed from these images.

based approach, it is assumed that the brain is a symmetrical structure and the difference between the left and right hemispheres is used to detect the lesions. The limitation of this approach is that the human brain is not perfectly symmetric [11], which affects the automatic detection process. In the template-based approach, a reference structure is formed from a group of healthy subjects data, and each subject volume is compared against this reference image to detect any abnormalities. The shortcoming of this method is that its accuracy depends on the normalization and registration steps (done as preprocessing) and are not suitable for children with developing brains [12]. In the feature-based approaches, suitable features that distinguish an FCD lesion from a normal region are learned. Mainly three types of features are studied from the subject data such as cortical thickness, blurring of gray matter-white matter junction, and increased FLAIR signal intensity. Based on these features, image processing methods, as well as machine learning approaches [13,8,14,10,15–18,12,19,20] were proposed in the literature. Recently a surface-based morphometry technique [21] that works across different 3 T MRI machines was proposed. Adler et al. in [12] developed an FCD method to detect FCD in children. The authors used a doughnut method to extract surface-based features other than the already established ones and are fed to a feed-forward neural network. A morphometry-based approach to detect MRI negative FCD lesions was recently proposed by Ahmed et al. [17]. In most of the aforementioned methods, their performance largely depends on the carefully designed human engineered features. However, finding all the features that distinguish FCD pixels from normal pixels is a difficult task. Also, the above-mentioned methods did a patient/region-wise quantitative evaluation which will not measure the true extent of detected FCD lesions. In this work, we proposed a method based on CNN that was trained to work with images acquired with both 1.5T and 3T scanners. The MR images acquired with different magnetic field strength have variations in signal intensity, noise level and fine morphological appearance which can be observed in Fig. 1(a) and (b) respectively. Most of the methods proposed earlier used either T1w or T2w or a combination of T1w or T2w with FLAIR. In this work we considered only the FLAIR images to detect and quantify FCD regions. This is because the hyper-intense regions due to FCD is more visible in FLAIR when compared to T1 or T2. Previous studies [22] also show that specialized MRI protocol like 3D FLAIR and Proton density (PD) sequences helps in the better detection and characterization of FCD lesions.

At present deep learning methods are the state-of-the-art approaches for different computer vision tasks such as classification, segmentation, object recognition, etc. [23]. CNN's are capable of learning themselves from labelled training images and later give an accurate prediction on test images provided. The ability to learn the appropriate features/representations from the training data without any human interventions makes the CNN the suitable method for addressing the limitations of conventional image processing/machine learning methods which required handcrafted features for classification. Also, CNN based methods are applied to a range of problems in MRI like brain tissue segmentation [24], prostate segmentation [25], Alzheimer's disease diagnosis [26], bi-ventricular volume estimation, [27] etc., and was a major motivation for carrying out this study. As far as we are aware, this work is the first one to use a CNN based model to detect and localize FCD lesions from MRI FLAIR images alone.

The rest of this paper is structured as follows: The detailed description of the proposed methodology is provided in Section 2. Section 3 discusses the experimental setup used in this work. The results and discussions are presented in Section 4. Finally, Section 5 summarizes and concludes the paper.

2. Methodology

The methodology used in this work consists mainly of three steps: pre-processing, FCD segmentation, and post-processing.

2.1. Preprocessing

The following pre-processing steps are applied first:

(i) Noise reduction: MRI images are generally corrupted by noise, which affects the automated segmentation process. So we first denoised the images to improve its SNR. The acquired MRI images are denoised with the state-of-the-art BM3D algorithm (for Rician noise). We used the methods proposed in [28,29] for this purpose.

(ii) Skull-stripping: FCD lesions occur in the cortex of the brain, and hence the region of interest (ROI) is limited to the brain. We used FSL-BET toolbox [30] to perform the skull-stripping operation to restrict our ROI to the brain region.

A sample noisy MRI frame, it's corresponding denoised image and skull stripped result is shown in Fig. 2(a)–(c) respectively.

2.2. FCD lesion segmentation

The lesion segmentation is achieved using a special kind of CNN called fully convolutional neural network (FCN) [31]. The advan-
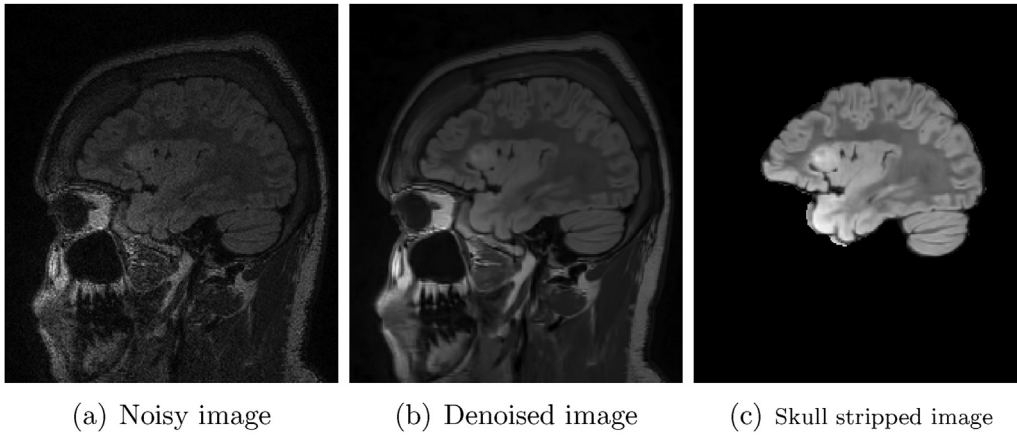
(a) Noisy image   (b) Denoised image   (c) Skull stripped image

Fig. 2. Preprocessing steps on a sample MRI frame.

tage of FCN is that it does not contain any fully connected layer or multilayer perceptron (MLP) at the end of the network and hence produces an output image of the same size as the input. Each pixel in the output image represents a prediction score which is converted to the required binary segmentation map.

In this work, we have used a customized version of U-Net architecture [32]. U-Net architecture is similar to an auto-encoder model where it has contracting and expanding paths. Unlike the auto-encoder, U-Net predicts a pixel-by-pixel segmentation map rather than an image as a whole.

2.3. Network architecture

The architecture used in our work is shown in Fig. 3. The model takes an input image of size 256×256. In the contracting path, each block consists of two 3×3 convolutional layers followed by a Rectified Linear Unit (ReLU) activation function [33]. Then the resultant output of each block is feed into a batch normalization layer (BN) [34]. After the batch normalization in the contracting path, a 2×2 max pooling operation is performed. To compensate for the loss of spatial information due to max pooling, the number of filters in the convolutional layer of subsequent blocks are doubled. In the expanding path, the spatial dimension of the feature maps is increased by a transposed convolutional operation [35]. Then, high-resolution feature maps from the contracting path are concatenated to the upsampled resultant image. In order to further reduce the effect of overfitting and co-adaption of intermediate features, we used the dropout [36] technique after the concatenation step. The dropout probability that we used is 0.2. Finally, a 1×1 convolution layer with sigmoid activation is performed at the last layer of the network. Hence, the resultant output image size will be the same as that of the input, and each pixel value corresponds to a probability value which is then thresholded to convert to the required binary segmentation map.

The loss function used to train the model is a combination of Binary Cross-Entropy function and the Dice loss and can be written as:

$$loss = BCE + DL \tag{1}$$

where BCE is the Binary Cross-Entropy and is defined as [37]:

$$BCE = -\sum_{i=1}^{N} \left(\psi_i \log(\phi_i) + (1 - \psi_i) \log(1 - \phi_i) \right) \tag{2}$$

where N is the total number of pixels in a single image and ψ_i and ϕ_i represents the actual ground truth and prediction for the pixel i respectively. DL is the Dice loss and is defined as [38]

$$DL = 1 - \frac{\sum_{i=1}^{N} \phi_i \psi_i + \epsilon}{\sum_{i=1}^{N} \phi_i + \psi_i + \epsilon} - \frac{\sum_{i=1}^{N} (1 - \phi_i)(1 - \psi_i) + \epsilon}{\sum_{i=1}^{N} 2 - \phi_i - \psi_i + \epsilon} \tag{3}$$

where ϵ is a constant used to avoid divide by zero error.

Adam optimizer [39] is used to update the weights. The learning rate used is 0.001 with a batch size of 32 which is empirically found using a random search. Weights of the network were initialized using Xavier uniform initializer [40] and bias is initialized to 0. The initialized weight W, is drawn from a uniform distribution which is defined as [40]:

$$W \epsilon U \left[-\sqrt{\frac{6}{c_{input} + c_{output}}}, \sqrt{\frac{6}{c_{input} + c_{output}}} \right] \tag{4}$$

where c_{input} and c_{output} are the size of input and output of the corresponding convolutional layer respectively.

Two or more layers are stacked together in the proposed model so that the output of $(k-1)$th layer is fed as input to the kth layer. All the convolution operation is done by zero-padding the image in order to preserve the spatial dimension of the image. All the convolutional filters have the size of 3×3. This filter size is chosen to keep the model parameters small without compromising the receptive field of the filter [41]. The model was trained from scratch and to reduce the over-fitting, real-time data augmentation is applied during the training. The transformations used for data augmentation are horizontal flips, rotation, and zooming. These transformations are performed in real-time during the training process which reduces the storage requirement. The model is trained for 100 epochs, and the learning rate is reduced by a factor of 0.4 when the validation loss stops improving.

2.4. Post-processing

The output of the model undergoes a post-processing operation using an average filter with a stride of 1. This operation is performed to reduce the false positive pixels and miss-detections in our model. We applied this averaging filter to the binary output, and the resulting values are rounded to get the final binarized segmentation map. After experimenting with different filter sizes, we choose a filter size of 5×5 by comparing the results between the enhanced prediction segmentations and the ground truth labels.
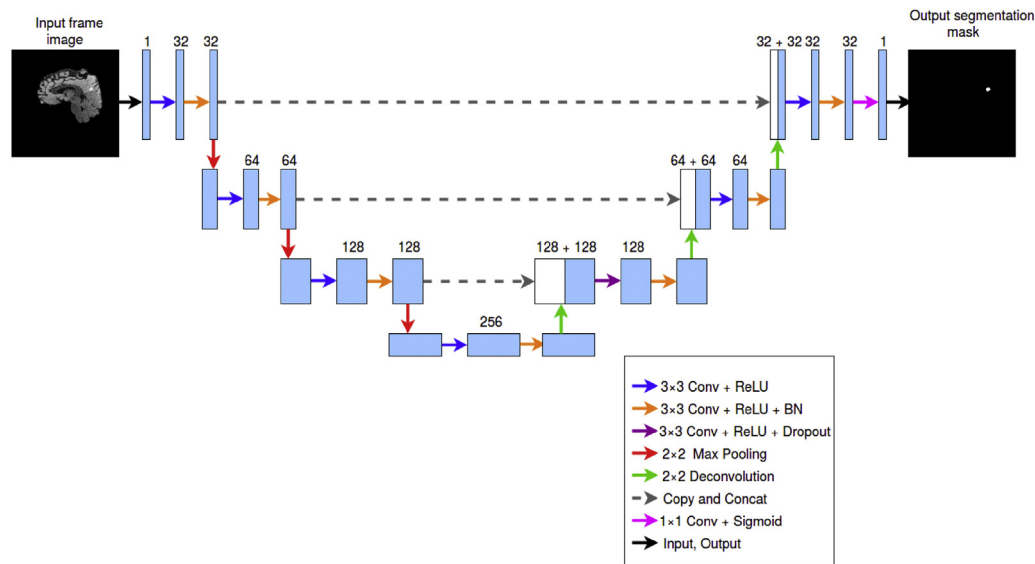
Fig. 3. Proposed FCN model for FCD lesion segmentation.

3. Experimental setup

The evaluation of the proposed method is done on the dataset collected from Sree Chitra Tirunal Institute for Medical Sciences and Technology (SCTIMST), Trivandrum, India. This study was approved by the SCTIMST institutional ethics committee review board. Keras, with Tensorflow [42] as back-end was used to implement the proposed method. All experiments are performed on a workstation with a 64-bit Ubuntu 18.04 OS, Intel Xeon(R) Gold 5120 CPU @ 2.20 GHz × 28, solid state hard drive, 64 GB of RAM and NVIDIA Quadro P500 GPU with 16 GB dedicated memory. Both quantitative and qualitative analysis of the proposed method has been done and are discussed in Section 4.

3.1. Dataset description

3D FLAIR weighted sequence images (of 43 subjects) were selected by the neuroradiologists in this retrospective study. All these subjects suffer from intractable epilepsy due to FCD. These selected subjects have undergone a specialized epilepsy protocol study for FCD during the period of April 2010–November 2018. This data was given to the computer-scientist after anonymizing the patient details. Out of the 43 subjects, 26 were acquired using a 3 T MRI machine and rest 17 with the 1.5 T machine.

The MR images acquired using the 1.5 T scanner (Siemens Medical Systems, Germany) contains a varying number of slices ranging between 144 and 192 with TR/TE/TI/flip angle of 5000 ms/333 ms/1800 ms/120°. All these images were acquired in the sagittal plane with a matrix size of 256 × 224, thickness 1 mm and pixel spacing 1.01 mm. While the images obtained on 3 T scanner (GE Healthcare, United Kingdom) were captured in the sagittal plane and contains a uniform number of 320 slices per subject with every slice having a size of 512 × 512 matrix and TR/TE/TI/flip angle of 7200 ms/117.241 ms/1936 ms/90° with thickness 1 mm and pixel spacing 0.5 mm. A sample MRI frame from both MRI scanners is shown in Fig. 1.

Since all the volumes in the dataset were acquired along the sagittal plane, the images had the highest resolution in that plane. Due to this reason, the proposed CNN model is trained on sagittal frames. The starting and ending frames in each MRI volumes contain blank frames or frames with fewer brain pixels. So we have excluded them from making the final dataset.

Table 1
Dataset description in terms of MRI frames. The values in brackets show the number of volumes.

Subset of data	Training	Validation	Testing
3 T	4302 (18)	1075 (4)	1194 (4)
1.5 T	1378 (10)	344 (3)	586 (4)
Total	5680 (28)	1419 (7)	1780 (8)

3.2. Training the model

The whole dataset (2D frames from 3D volumes) is divided into train and test set based on the 80–20% rule. For finding the optimal hyperparameters of the proposed FCN, we employed a holdout approach for the model validation which constitutes a train data of ~5680 frames, validation data of ~1419 frames and test data of ~1780 frames acquired with 1.5T and 3T machines. Since our test set is relatively small, we used 5-fold cross-validation to avoid statistical uncertainty. While forming all the folds, we made sure that the train, test, and validation frames are taken from unique patients and there would not be any biased test frames for performance evaluation. Also while creating training, validation and test set, we made sure that all the 3 sets contain an appropriate number of frames with and without FCD. Out of 8849 frames, 1431 were FCD positives and we divided the positive frames as follows. 65% for training, 17% for validation and 18% for testing. Table 1 shows the volume-wise dataset distribution of images acquired with both 1.5T and 3T machines. After applying the preprocessing operations mentioned in Section 2.1, only the region of interest, i.e., the brain region alone was considered for the FCD lesion segmentation. All images are then resized to a uniform resolution of 256 × 256 using bilinear interpolation. After resizing, all frames are normalized to zero mean and unit variance [41].

The training process for different FCN models with varying depths is shown in Fig. 4. Table 2 depicts the details of these models. The term depth, parameters, and layers refer to the number of max-pooling layers, weights, and convolutional layers respectively. It can be observed from the plots in Fig. 4 that the model with depth 3 fits better when compared to other models. We can see that the difference between training and validation loss is less in the model with depth 3. Next, the effect of the receptive field is explored. The receptive field represents the effective area covered in the input image by the convolutional filter. A smaller filter size
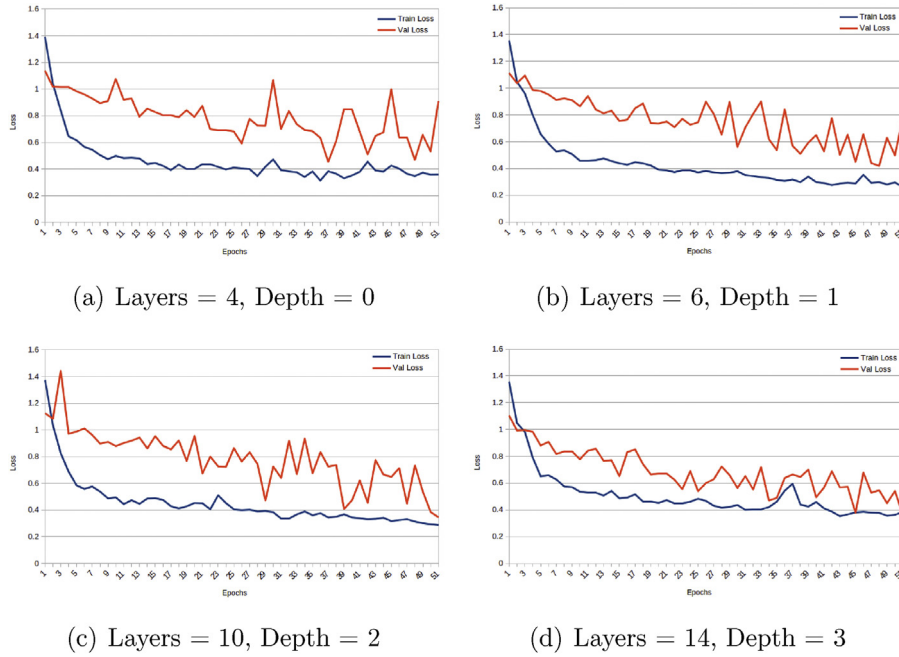
(a) Layers = 4, Depth = 0   (b) Layers = 6, Depth = 1

(c) Layers = 10, Depth = 2   (d) Layers = 14, Depth = 3

Fig. 4. Loss curves of FCN models by varying depths.

Table 2
Parameter details of FCN models at depths.

Depth	No. of layers	No. of filters (k)	Filter size ($w \times h$)	Total no. of parameters
0	4	64	3×3	112,513
1	6	64	3×3	367,809
2	10	64	3×3	1,866,817
3	14	64	3×3	7,707,457

Table 3
Parameter details of FCN models by varying starting filter size in depth 3.

No. of filters (k)	Filter size ($w \times h$)	Total no. of parameters
64	3×3	7,707,457
32	3×3	1,930,657
16	3×3	484,561

helps in learning minute features of FCD, and by stacking two or more smaller convolutional filters, a bigger receptive field can be achieved without increasing the number of parameters [41]. Hence, all the convolutional filters have the size of 3×3.

Further, keeping depth 3 as constant, the number of starting convolutional filters are varied. Table 3 shows the total number of parameters of various models formed by changing the starting filter size. Fig. 5(a)–(c)shows the corresponding training process. We can observe from Fig. 5 that the starting filter with 32 is more generalizable and exhibit less overfitting trend. Fig. 6 shows the loss curves of the proposed model during the training phase in which the blue and red descending curves depict the loss function values for the training and the validation sets respectively (average of 5 experiments). To train 5680 samples of data, the proposed model took 91 seconds per epoch and for prediction of 1780 test samples, 0.03 seconds per test image was taken.

4. Results and analysis

The performance of the proposed method is evaluated both qualitatively and quantitatively. For quantitative evaluation, we did patient-wise, region-wise and pixel-wise analysis. We used preci-

sion, recall and Dice coefficient for quantitative analysis. Precision is the ratio of the True Positives (TP) to the sum of TP and False Positives (FP) where TP is the actual lesion pixels that are identified by the model and FP are the pixels that are identified by the model which are not a part of the actual lesion. The recall is the ratio of TP to the sum of TP and False Negatives (FN) where FN is the actual lesion pixels unidentified by the model. Precision and recall metrics are calculated as:

$$Precision = \frac{TP}{TP + FP} \tag{5}$$

$$Recall = \frac{TP}{TP + FN} \tag{6}$$

We also used the Dice coefficient [43] to determine the correlation accuracy of the segmentation and is defined as:

$$Dice coefficient = 2 \times \frac{Precision \times Recall}{Precision + Recall} \tag{7}$$

Figs. 7 and 8 show the qualitative analysis of the proposed FCN method. The images in Fig. 7 shows five continuous slides from two different patients with FCD. The first, second and third column of the images represent the original scans, labelled ground truth, and prediction of the proposed segmentation method. It can be observed from the figure that the FCD lesions are correctly detected and segmented by the proposed method. In some cases, the method was not that accurate in extracting the true extent of the FCD regions.

The limiting results of the FCN model are shown in Fig. 8. In the first case, the model failed to identify the FCD regions and in the second case, it could not properly segment the entire lesion. This is because there was less variation in the intensity between the lesion pixels and the neighboring normal ones. The inter-class similarity (between FCD and normal region) was also very high in such cases.

The pixel-wise analysis of the proposed method with and without post-processing is reported in Table 4. It can be noticed from the table that post-processing improved the performance of the method. We used an average filter of size 5×5 for post-processing and that helped in reducing the false positives and miss detections. The post- processing improves the recall rate by 8%, precision by 2% and the Dice value by 6%. We also compared the performance of
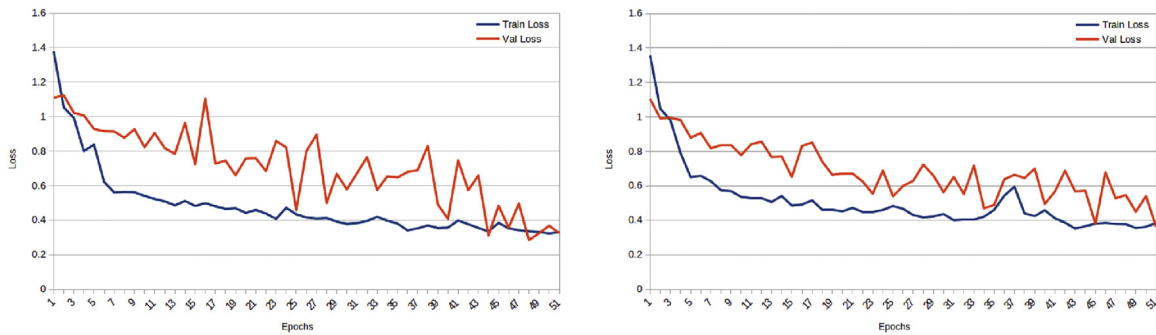
(a) Starting Filter Size k = 16

(b) Starting Filter Size k = 32
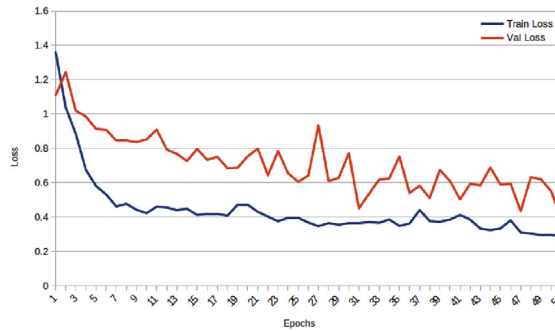
(c) Starting Filter Size k = 64

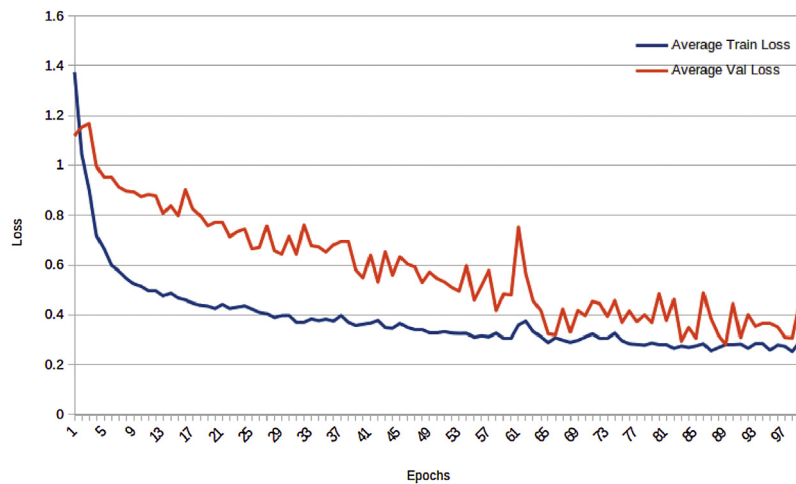**Fig. 5.** Loss curves of FCN models formed by varying starting filter sizes in depth 3.

Fig. 6. Loss curves of the proposed model during training phase (mean of 5 experiments).

Table 4
Pixel-wise evaluation of proposed method with and without post-processing.

	Recall	Precision	Dice coefficient
Without post-processing	37.06	79.28	49.47
With post-processing	40.10	80.69	52.47

the proposed method with other state-of-the-art approaches. For comparison, we used the results reported in the respective papers. The patient-wise analysis with recently published methods shows that the proposed method is superior in identifying the FCD lesions. The proposed method has a recall rate of 82.5 (33/40) in identifying the FCD from the given MRI volumes. To measure the robustness of the proposed method we also did region-wise and pixel-wise analysis. The proposed model also shows better pixel-wise detection performance while comparing with other approaches. The results reported in the table shows that the proposed method is capable of detecting the FCD and identifying the extent of FCD region (Table 5).

5. Discussions and conclusion

This work presents an FCN model-based automated FCD lesion segmentation technique which works on MRI images acquired with both 1.5T and 3T scanners. The proposed model is trained from scratch using the denoised and skull-stripped MRI scans and customized for FCD lesion segmentation. Moreover, data augmen-
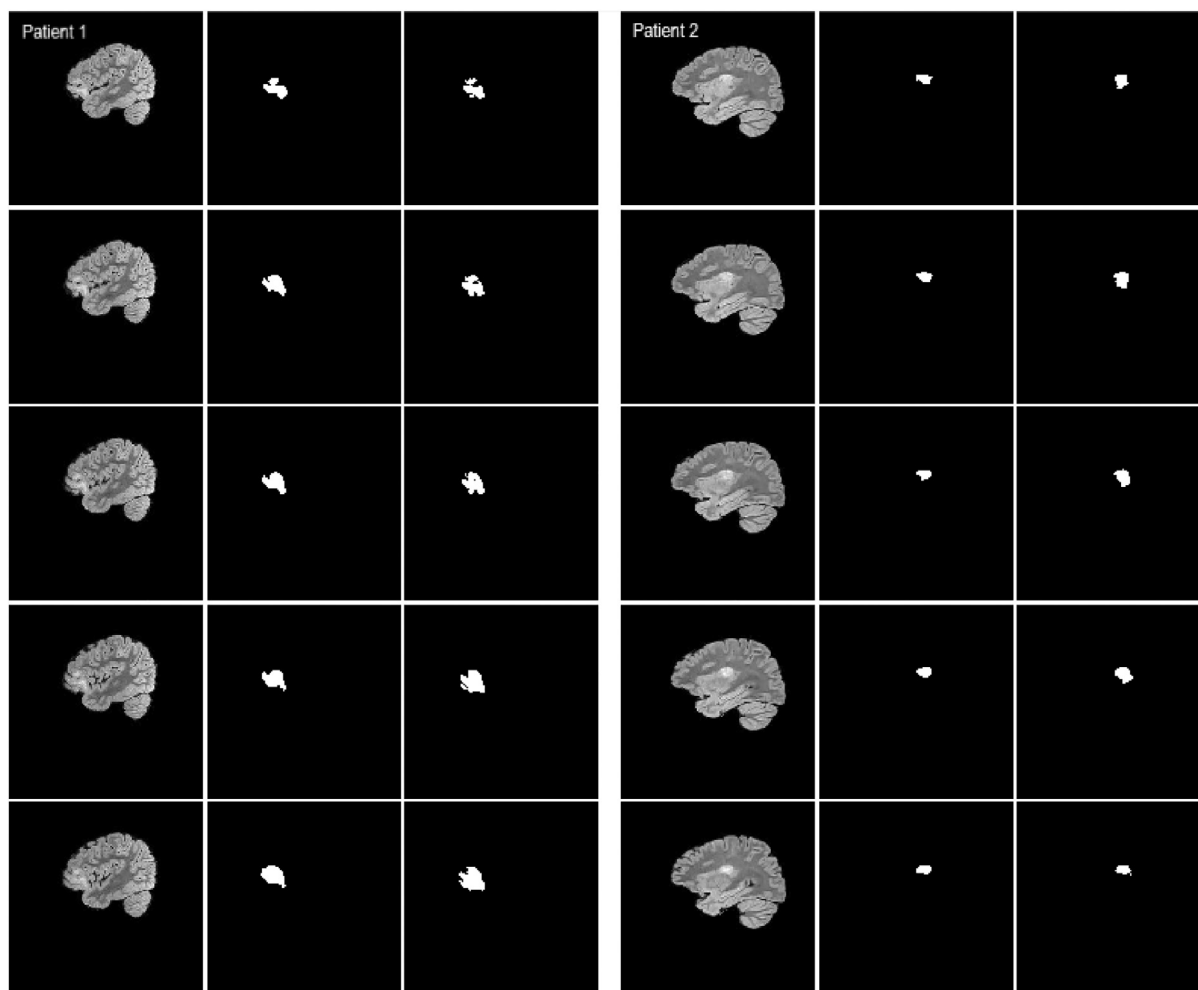
Fig. 7. Segmentation results of the proposed method on MRI scans of two patients with FCD. The first column in the images is the MRI scan with FCD, the second column is the Ground Truth and the third column is the predicted output.
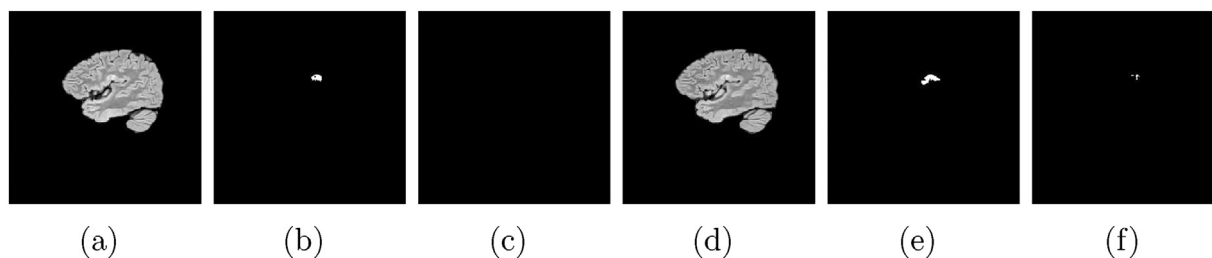

Fig. 8. Segmentation results showing the limitation of the proposed technique on various MRI scans against the Ground Truth. (a) and (d) are the MRI scans with FCD, (b) and (e) are the Ground Truth, (c) and (f) are the Predicted outputs.

Table 5
Performance evaluation of the proposed method with state-of- the-art methods in terms of precision, recall and dice coefficient.

Related works	Patient-wise	Region-wise		Pixel-wise		
	Recall	Recall	Precision	Recall	Precision	Dice coefficient
Ahamed et al. [17]	58	–	–	20.1	27.67	20.30
Pascal et al. [44]	55	–	–	–	–	–
Proposed method	**82.5**	**48**	**89**	**40.1**	**80.69**	**52.47**

tation techniques play a significant role in training the model by increasing the amount of the training data in real-time by rotating, zooming and horizontally flipping the training samples thereby reducing the chance of overfitting. FCD lesions are highly variable in their spatial localization, and structural composition. Data augmentation techniques were quite effective to cope with such variability. The proposed FCN model is built with 3×3 kernels in all convolutional layers to have higher receptive field and deeper architecture.

The performance of the model was evaluated both qualitatively and quantitatively and the comparative analysis shows that the proposed method is superior in terms of the measures that we used. The proposed automated method can be a valuable tool that helps the neuroradiologists in pre-surgical evaluation of patients with intractable epilepsy. The proposed framework can be easily adapted for the detection and localization of other kinds of lesions in the brain. As a whole, our method is a strong candidate for FCD lesion identification/segmentation using MRI images which may help to increase the accuracy of surgical outcome in intractable epilepsy patients.

Acknowledgement

References

[1] E. Foundation, About Epilepsy: The Basics, accessed: 2018-04-07, https://www.epilepsy.com/learn/.
[2] R. Dingledine, B. Hassel, A new approach for epilepsy, in: Cerebrum: The Dana Forum on Brain Science, vol. 2016, Dana Foundation, 2016.
[3] J. Kabat, P. Król, Focal cortical dysplasia – review, Pol. J. Radiol. 77 (2) (2012) 35.
[4] V. Alexandre, R. Walz, M.M. Bianchin, T.R. Velasco, V.C. Terra-Bustamante, L. Wichert-Ana, D. Araújo, H.R. Machado, J.A. Assirati, C.G. Carlotti, et al., Seizure outcome after surgery for epilepsy due to focal cortical dysplastic lesions, Seizure-Eur. J. Epilepsy 15 (6) (2006) 420–427.
[5] J.S. Hauptman, G.W. Mathern, Surgical treatment of epilepsy associated with cortical dysplasia: 2012 update, Epilepsia 53 (s4) (2012) 98–104.
[6] S.L. Simpson, R.A. Prayson, Post-surgical outcome for epilepsy associated with type I focal cortical dysplasia subtypes, Mod. Pathol. 27 (11) (2014) 1455.
[7] R.I. Kuzniecky, A.J. Barkovich, Malformations of cortical development and epilepsy, Brain Dev. 23 (1) (2001) 2–11.
[8] J. Rajan, K. Kannan, C. Kesavadas, B. Thomas, Focal cortical dysplasia (FCD) lesion analysis with complex diffusion approach, Comput. Med. Imaging Graph. 33 (7) (2009) 553–558.
[9] S.B. Antel, A. Bernasconi, N. Bernasconi, D.L. Collins, R.E. Kearney, R. Shinghal, D.L. Arnold, Computational models of MRI characteristics of focal cortical dysplasia improve lesion detection, Neuroimage 17 (4) (2002) 1755–1760.
[10] C.-A. Yang, M. Kaveh, B.J. Erickson, Automated detection of focal cortical dysplasia lesions on t1-weighted MRI using volume-based distributional features, 2011 IEEE International Symposium on Biomedical Imaging: From Nano to Macro, IEEE (2011) 865–870.
[11] T.J. Crow, J. Ball, S.R. Bloom, R. Brown, C.J. Bruton, N. Colter, C.D. Frith, E.C. Johnstone, D.G. Owens, G.W. Roberts, Schizophrenia as an anomaly of development of cerebral asymmetry: a postmortem study and a proposal concerning the genetic basis of the disease, Arch. Gen. Psychiatry 46 (12) (1989) 1145–1150.
[12] S. Adler, K. Wagstyl, R. Gunny, L. Ronan, D. Carmichael, J.H. Cross, P.C. Fletcher, T. Baldeweg, Novel surface features for automated detection of focal cortical dysplasias in paediatric epilepsy, NeuroImage: Clin. 14 (2017) 18–27.
[13] B.N.N.V.K.D, O. Colliot, Mansi T.,B.A, Segmentation of focal cortical dysplasia lesions on MRI using level set evolution, Neuroimage 32 (4) (2006) 1621–1630.
[14] P. Besson, O. Colliot, A. Evans, A. Bernasconi, Automatic detection of subtle focal cortical dysplasia using surface-based features on MRI, 5th IEEE International Symposium on Biomedical Imaging: From Nano to Macro, 2008, ISBI 2008, IEEE (2008) 1633–1636.
[15] M. El Azami, A. Hammers, N. Costes, C. Lartizien, Computer aided diagnosis of intractable epilepsy with MRI imaging based on textural information, 2013 International Workshop on Pattern Recognition in Neuroimaging (PRNI), IEEE (2013) 90–93.
[16] S.-J. Hong, H. Kim, D. Schrader, N. Bernasconi, B.C. Bernhardt, A. Bernasconi, Automated detection of cortical dysplasia type II in MRI-negative epilepsy, Neurology 83 (1) (2014) 48–55.
[17] B. Ahmed, C.E. Brodley, K.E. Blackmon, R. Kuzniecky, G. Barash, C. Carlson, B.T. Quinn, W. Doyle, J. French, O. Devinsky, et al., Cortical feature analysis and machine learning improves detection of "MRI- negative" focal cortical dysplasia, Epilepsy Behav. 48 (2015) 21–28.
[18] M. El Azami, A. Hammers, J. Jung, N. Costes, R. Bouet, C. Lartizien, Detection of lesions underlying intractable epilepsy on t1-weighted MRI as an outlier detection problem, PLOS ONE 11 (9) (2016) e0161498.
[19] N.K. Focke, M.R. Symms, D.J.S, Voxel-based analysis of whole brain flair at 3T detects focal cortical dysplasia, Epilepsia 49 (5) (2008) 786–793.
[20] Y.M.S.C.S.M, N.K. Focke, S.B. Bonelli, D.J.S, Automated normalized flair imaging in MRI-negative patients with refractory focal epilepsy, Epilepsia 50 (6) (2009) 1484–1490.
[21] B. Jin, B. Krishnan, S. Adler, K. Wagstyl, W. Hu, S. Jones, I. Najm, A. Alexopoulos, K. Zhang, J. Zhang, M. Ding, S. Wang, N. Pediatric Imaging, t. Genetics Study, Z. Irene Wang, Automated detection of focal cortical dysplasia type II with surface-based magnetic resonance imaging postprocessing and machine learning.
[22] J. Saini, A. Singh, C. Kesavadas, B. Thomas, C. Rathore, B. Bahuleyan, A. Radhakrishnan, K. Radhakrishnan, Role of three-dimensional fluid-attenuated inversion recovery (3D flair) and proton density magnetic resonance imaging for the detection and evaluation of lesion extent of focal cortical dysplasia in patients with refractory epilepsy, Acta Radiol. 51 (2) (2010) 218–225.
[23] Y. LeCun, Y. Bengio, G. Hinton, Deep learning, Nature 521 (7553) (2015) 436.
[24] P. Moeskops, M.A. Viergever, A.M. Mendrik, L.S. de Vries, M.J. Benders, I. Išgum, Automatic segmentation of MR brain images with a convolutional neural network, IEEE Trans. Med. Imaging 35 (5) (2016) 1252–1261.
[25] Y. Guo, Y. Gao, D. Shen, Deformable MR prostate segmentation via deep feature learning and sparse patch matching, in: Deep Learning for Medical Image Analysis, Elsevier, 2017, pp. 197–222.
[26] E. Hosseini-Asl, R. Keynton, A. El-Baz, Alzheimer's disease diagnostics by adaptation of 3D convolutional network, in: 2016 IEEE International Conference on Image Processing (ICIP), IEEE, 2016, pp. 126–130.
[27] X. Zhen, Z. Wang, A. Islam, M. Bhaduri, I. Chan, S. Li, Multi-scale deep networks and regression forests for direct bi-ventricular volume estimation, Med. Image Anal. 30 (2016) 120–129.
[28] M. Maggioni, V. Katkovnik, K. Egiazarian, A. Foi, Nonlocal transform-domain filter for volumetric data denoising and reconstruction, IEEE Trans. Image Process. 22 (1) (2013) 119–133.
[29] M. Maggioni, A. Foi, Nonlocal transform-domain denoising of volumetric data with groupwise adaptive variance estimation, Computational Imaging X, vol. 8296, International Society for Optics and Photonics (2012), p. 82960O.
[30] S.M. Smith, Fast robust automated brain extraction, Hum. Brain Mapping 17 (3) (2002) 143–155.
[31] J. Long, E. Shelhamer, T. Darrell, Fully convolutional networks for semantic segmentation, Proceedings of the IEEE Conference on Computer Vision and Pattern Recognition (2015) 3431–3440.
[32] O. Ronneberger, P. Fischer, T. Brox, U-net: convolutional networks for biomedical image segmentation, in: International Conference on Medical Image Computing and Computer-Assisted Intervention, Springer, 2015, pp. 234–241.
[33] V. Nair, G.E. Hinton, Rectified linear units improve restricted Boltzmann machines, Proceedings of the 27th International Conference on Machine Learning (ICML-10) (2010) 807–814.
[34] S. Ioffe, C. Szegedy, Batch normalization: accelerating deep network training by reducing internal covariate shift, International Conference on Machine Learning (2015) 448–456.
[35] H. Noh, S. Hong, B. Han, Learning deconvolution network for semantic segmentation, Proceedings of the IEEE International Conference on Computer Vision (2015) 1520–1528.
[36] N. Srivastava, G. Hinton, A. Krizhevsky, I. Sutskever, R. Salakhutdinov, Dropout: a simple way to prevent neural networks from overfitting, J. Mach. Learn. Res. 15 (1) (2014) 1929–1958.
[37] J. Shore, R. Johnson, Axiomatic derivation of the principle of maximum entropy and the principle of minimum cross-entropy, IEEE Trans. Inf. Theory 26 (1) (1980) 26–37.
[38] C.H. V.T.O.S. Sudre, W.C.M.J. Li, Generalised dice overlap as a deep learning loss function for highly unbalanced segmentations, Deep Learning in Medical Image Analysis and Multimodal Learning for Clinical Decision Support (2017) 240–248.
[39] D.P. Kingma, J. Ba, Adam: a method for stochastic optimization, arXiv preprint arXiv:1412.6980.
[40] X. Glorot, Y. Bengio, Understanding the difficulty of training deep feedforward neural networks, Proceedings of the Thirteenth International Conference on Artificial Intelligence and Statistics (2010) 249–256.
[41] A. Karpathy, Cs231n convolutional neural networks for visual recognition, Neural Netw. 1 (2016).
[42] F. Chollet, et al., Keras, 2015.
[43] L.R. Dice, Measures of the amount of ecologic association between species, Ecology 26 (3) (1945) 297–302.
[44] P. Martin, G.P. Winston, P. Bartlett, J. de Tisi, J.S. Duncan, N.K. Focke, Voxel-based magnetic resonance image postprocessing in epilepsy, Epilepsia 58 (9) (2017) 1653–1664.